## ORIGINALS

C.-T. Yang · H.-S. Chuang

# Measurement of a microchamber flow by using a hybrid multiplexing holographic velocimetry

**Abstract** A hybrid multiplexing holographic velocimetry used for characterizing three-dimensional, three-component (3D–3C) flow behaviors in microscale devices was designed and tested in this paper. Derived from the concept of holographic particle image velocimetry (HPIV), a new experimental facility was realized by integrating a holographic technique with a state-of-the-art multiplexing operation based on a microPIV configuration. A photopolymer plate was adopted as an intermedium to record serial stereoscopic images in the same segment. The recorded images were retrieved by a scanning approach, and, afterwards, the distributions of particles in the fluid were analyzed. Finally, a concise cross-correlation algorithm (CCC) was used to analyze particle movement and, hence, the velocity field, which was visualized by using a chromatic technique. To verify practicability, the stereoscopic flow in a backward facing step (BFS) chamber was measured by using the new experimental setup, as well a microPIV system. The comparison indicated that the photopolymer-based velocimetry was practicable to microflow investigation; however, its accuracy needed to be improved.

## 1 Introduction

Many techniques have been developed to explore three-dimensional (3-D) flows in wind tunnels, combustion engines, pipelines, etc. However, the innovation of measurement techniques is still necessary to meet the requirements for understanding flow charac-

C.-T. Yang (✉) · H.-S. Chuang
Center for Measurement Standards, Industrial Technology
Research Institute, No. 30 Ta-Shueh Rd.,
Hsinchu, 300, Taiwan
E-mail: ctyang@itri.org.tw
Tel.: +886-3-5741206
Fax: +886-3-5710335

teristics in microscale devices. Santiago et al. (1998) were the first to employ a microresolution particle image velocimetry (microPIV) to investigate microflow. Although the technique has been widely adopted in acquiring microflow information plane by plane, a new technique that could explore transient full-field 3-D flow is still in urge.

The developed measurement systems for macro 3-D flow are based mainly on color-coded (Kawahashi and Hirahara 2001) or multi-camera (Clark 1973) techniques. Holography, another alternative, records both the intensity and phase of the interfered flow images. Afterward, the stereoscopic images can then be retrieved and analyzed in order to obtain the 3-D flow information. This kind of holographic particle image velocimetry (HPIV) system is widely used and has made great progress (Coupland and Halliwell 1992; Barnhart et al. 1994; Zhang et al. 1997; Royer 1997; Lozano et al. 1999; Arroyo et al. 2000; Hinsch 2002). An example would be Schnars and Jüptner's (1994) proposal of a digital holography (DH) using a high-resolution charge coupled device (CCD) chip, which was used to replace holographic elements so that complicated wet processing can be avoided. The digital HPIV (DHPIV) technique has shown its feasibility to real-time flow measurements; however, the performance was restricted by low CCD resolution (< 100 lp/mm) and high speckle noise. Derived from the techniques of DHPIV, many new developments (Cuche et al. 1999; Dubois et al. 1999; Pan and Meng 2001; Xu et al. 2001) have shown their applicability in 3-D microscopic fluidic diagnoses. Aside from this, forward-scattering particle image velocimetry (FSPIV) (Ovryn 2000) is also a potential solution in which particle locations are deduced from the measured diffraction patterns. This application of FSPIV gets rid of the use of expensive coherent light sources; however, the discrimination of overlapped particles is impeded by serious cross talk.

In this paper, a new experimental method was introduced, which incorporated microscopy, photo-

polymers, and multiplex exposure operations. First, images of the microchannel flow were magnified and transmitted via the microscopy. Sequential volume holograms were then stored in a high-sensitivity photopolymer by using a hybrid multiplexed optical operation. Afterwards, the 3-D microflow field was obtained from the retrieved holograms by using a concise cross-correlation (CCC) algorithm. To verify the practicability of the setup, the free flow in a straight microchannel seeded with 1-μm particles was first measured, and was then analyzed by using the CCC algorithm, as well a particle tracking velocimetry (PTV) algorithm for comparison. Furthermore, the flow in a backward facing step (BFS) chamber was measured to further verify the practicability of the experimental setup. Finally, a chromatic technique was adopted in visualizing the measured flow. The measurement accuracy was evaluated by comparing it with the measurements of a calibrated microPIV. The results confirmed the practicability of the new setup, but the 9% difference should be reduced by eliminating the influential uncertainty sources.

## 2 Experiments

### 2.1 Experimental setup

A schematic diagram of the hybrid multiplexing holographic velocimetry is illustrated in Fig. 1. The coherent light source was emitted from a ND:YAG continuous-wave (CW) laser (200 mW, 532 nm, Lightwave) and was then passed through an electric shutter, which resulted in modulated pulse chains. An attenuator was placed in the light path to switch the three operation modes: recording, reading, and observation. Prior to the operation, the light intensity was lowered by adjusting the attenuator to align the image to the CCD. While recording and reading an image, the attenuator was switched off or turned to the lowest level in order to supply the recording material with sufficient power. The incident beam was split through the polarized beam splitter cube (PBS 1) into two polarized states ($p$ and $s$), one as an object beam and the other as a reference beam. The half-wave plate ahead of the PBS 1 was used to adjust the incident polarized angle into the PBS in order to obtain equal light intensity in the two split beams. The mechanical shutter behind the PBS 1 was used to block the object beam while reading images.

The object beam illuminated the fluid in the microdevice, which was mounted on an inverted microscopy (IX51, Olympus). The scattered light was then collected by an objective lens (40×, numerical aperture (NA) = 0.65, Olympus) and the image was magnified. When the light came out of the side port of the microscopy, the projected images was focused through a 1:1 transformation lens system, which was composed of two achromatic lenses with a focal length of 75 mm. The depth of field of the transformation system, which is the sum of the diffraction and the geometrical effects (Inoué and Spring 1997), was estimated to be 1.52 μm, based on the assumption of no magnification and deformation.

In the reference arm, we used a dove prism on a linear stage to compensate for the path difference while adjusting optical components, including the integration of the ferroelectric liquid crystal (FLC, 24.5×24 mm active area, 100-μs rise time at 25°C, 30% transmission at 500 nm, CRL OPT), the half-wave plate, the PBS cube (PBS 2), the rotating carrier stage (0.005°/pulse, maximal traveling angle: 30°/s, Skid-40Yaw, Sigma Koki Co., Tokyo, Japan). Some mirrors and lenses that were well arranged formed the mechanism for hybrid multiplexing, and will be illustrated below. Finally, the reference beam interfered with the object beam in the photopolymer and the interference pattern for instantaneous flow was recorded.

### 2.2 Hybrid multiplexing mechanism

To record successive image pairs in the photopolymer, the FLC shutter, the electric shutter, and the rotation stage were synchronized by using a synchronizer (four CHs, 1-ns resolution and jitter, RS232, Model 555, BNC), as seen in Fig. 1. In this study, a two-stage hybrid multiplexing technique was proposed for obtaining discrete image pairs for analysis. The first stage, based on the fast switching of light polarization, is for recording an image pair. As shown in Fig. 2, the incoming horizontally polarized beam is turned vertical if the FLC shutter is at the $s$ state, and is then reflected in PBS cube (labeled as Ref 1). In contrast, the polarization of the beam is kept horizontal at the $p$ state, and is then passed through the PBS (labeled as Ref 2). The half-wave plate rotates the polarization of Ref 2 to vertical, the same as Ref 1 and the object beam. Both Ref 1 and Ref 2 then interfere with the object beam successively to generate an image pair.

The second multiplexing is based on an angular operation. By rotating the recording medium with an increment of about 0.4° by using a rotating stage as seen in Fig. 1, the next image pair can then be recorded in the same segment of the photopolymer as that in the first stage. As depicted in Fig. 3, the first multiplexing can operate rapidly and is suitable for capturing an image pair (image 1:1 and 1:2), while the second multiplexing is a mechanical motion and is suitable for preparing memory inside the medium for the next image pair (image 2:1 and 2:2). By repeating the two multiplexing operations, serial image pairs can be stored in the photopolymer simultaneously.

### 2.3 Recording material and recording performance

To effectively capture the images of particles in motion, material with high sensitivity, high dynamic range, and
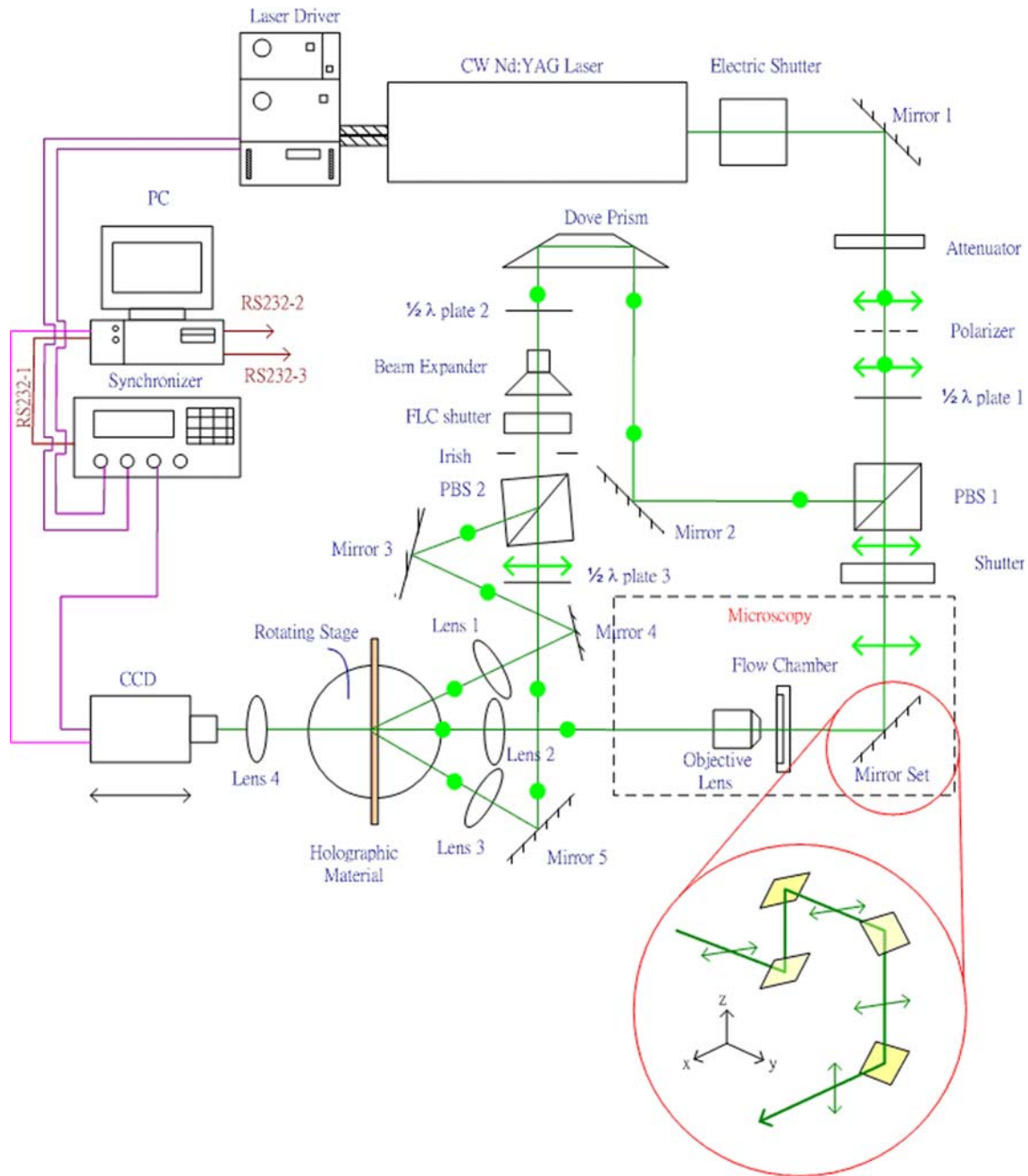
**Fig. 1** Schematic diagram of the hybrid multiplexing holographic velocimetry for 3-D microfluidic measurement

low shrinkage must be selected. Sensitivity defines the intensity needed for recording, while shrinkage defines the volume variation during recording, and the dynamic range determines how many holograms can be recorded. The dynamic range is defined as $M^{\#} = \sum_{i=1}^{M} \eta_i^{1/2}$, where $M$ is the number of holograms, and $\eta_i$ denotes the $i$th diffraction efficiency.

In our setup, CROP photopolymer (50×50 mm, card format, 300-μm thickness, centered at wavelength of 532 nm, Aprilis) was adopted because of its high sensitivity (2.29 cm/mJ), high dynamic range ($M^{\#} \sim 5.53$), and

low shrinkage ($< 0.1\%$). The CROP photopolymer is an organic material comprised of monomers, photosensitizers, and binders. The basic recording mechanism comes from the diffusion of monomers when the photosensitizers are activated via the illumination of green light (Paraschis et al. 1999; Waldman et al. 1998). The recording process was realized in a dark room treated with red light (RoscoLux SuperGel#27) because of the high sensitivity. Plus, though several tens of image pairs were stored, only a partial area of the material was consumed so that the rest of space was flooded with daylight for fixing the images.

Recording performance is another key factor in successful holography experiments. Two exposure strategies

**Fig. 2** Illustration of the polarizing switch mechanism. Ref 1 and Ref 2 are split due to their polarization states and are selected by the PBS cube spontaneously
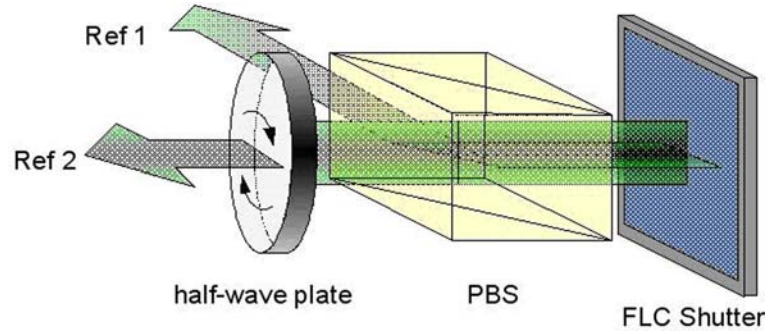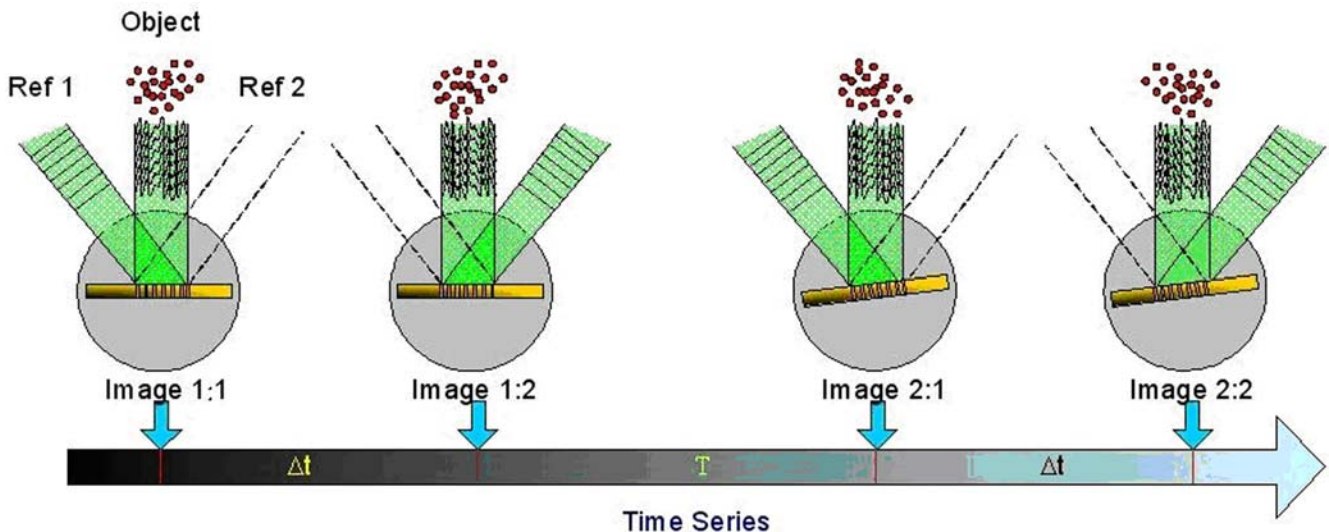
are generally applied to multiplexing holography: constant refraction and constant exposure. According to the dynamic range $M^{\#}$ in Fig. 4, the recording effect of the CROP photopolymer decreases nonlinearly with the same energy in successive recording. This indicates that CROP absorbs energy rapidly in the beginning, and approaches saturation soon after about 90% capacity is depleted. To achieve constant refraction, increasing the exposure time in the order according to the following equation (Ken et al. 2003) can maintain constant diffraction efficiency in each hologram:

$$t_n = \frac{1}{I}\frac{E_\tau}{N}\exp\left(\frac{1}{E_\tau}\sum_{i=1}^{N-1}E_i\right) \tag{1}$$

where $N$ is the desired number of exposures, $E_i$ is the exposure energy of the $i$th hologram, $E_\tau$ is the characteristic exposure energy, and $I$ is the incident light intensity. Alternatively, for constant exposure, the exposure time remains constant throughout the procedure, and, because of this, the diffraction efficiency decays with the number of recorded holograms.

Because the exposure energy, number of recordings, and exposure spot area were well controlled in advance, the constant exposure strategy was adapted in the present experiment. Figure 5 shows a dramatic trend of diffraction efficiency, where the initial energy per pulse is 11.1 mJ/cm$^2$ and the exposure area is 1.13 mm$^2$ . To get a similar diffraction efficiency for each hologram, the applied energy fluence and the spot size on the photopolymer was optimized. Figure 6 shows a case of fluence of 0.47 mJ/cm$^2$, with spot size 10.2 mm$^2$, in which the variation of diffraction efficiency among holograms is much improved. In practice, the evaluated number of recordings should be larger than expected to avoid the failing of recording due to overexposure, even at low fluence. Briefly, the constant exposure strategy benefitted from constant diffraction efficiency and, therefore, facilitated the recording process.

## 2.4 Retrieving images and reconstructing particle distribution

To retrieve the recorded images, the object beam was blocked and a CCD camera (B/W, 1,024×1,280 resolution, 6.7×6.7-μm pixel size, Pixefly 230XD, PCO) was placed behind the photopolymer plate. The holograms were retrieved plane by plane to form stereo images via

**Fig. 3** Illustration of the hybrid multiplexing. Time between each image in a pair ($\Delta t$) is much shorter than the time between two pairs ($T$). $\Delta t$ is determined by the first multiplexing operation and $T$ by the second
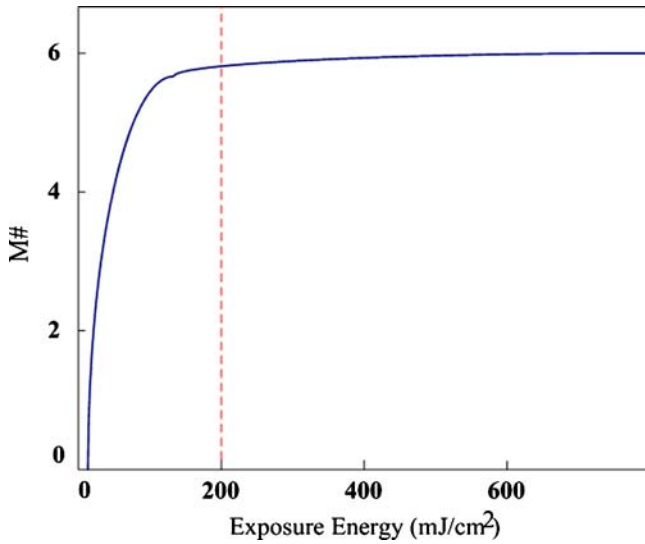
Fig. 4 A plot of cumulative grating strength versus exposure energy. The dynamic range ($M^{\#}$) approaches saturation while the total absorbing energy reaches 200 mJ/cm$^2$

a scanning arrangement. Following the same procedures as recording, images which reproduce the recorded fluid flow were collected and projected onto the CCD via a lens. While the CCD scanned along the optical axis by focusing on different image planes of each hologram, the spatial distribution of the particles was reconstructed from the retrieved sequential images via a CCC algorithm, which is explained further later. In the experiment, at least the early four to twelve holograms were read, although tens of holograms were memorized.

A CCC algorithm (Pu and Meng 2000; Pu 2002) was applied to extract the velocity distribution out of the reconstructed images. The particles were confirmed of its coordinates of centroids in advance. Then, as shown in Fig. 7, the correlation between the two images of an
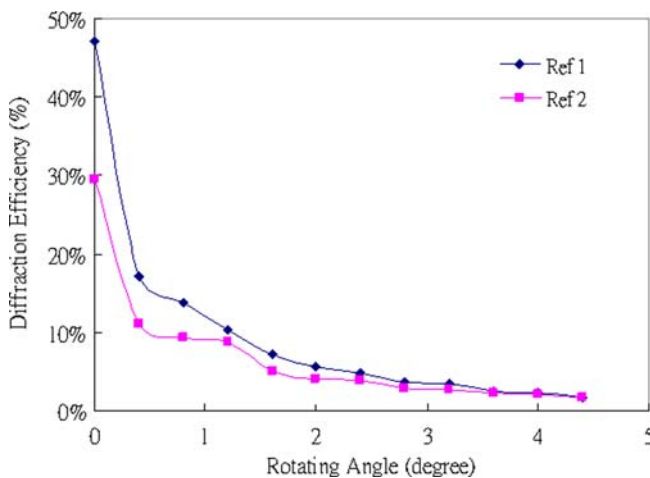
image pair was calculated by a statistical process as the second image was shifted a distance randomly. By comparing the calculated results in different shifts, the mean displacement of the particles between the two images was determined where the maximum correlation occurred. Assuming that all particles are well paired between two images, the displacements along the three axes can be determined individually, and this accelerates the displacement determination in comparison with the conventional algorithms, i.e., the computational complexity is simplified as:

$$f\left(N^2 D^3\right) \to f\left(N^2 D\right) \tag{2}$$

where $N$ denotes the images for cross correlation and $D$ denotes the dimensions in Cartesian coordinates.

The conventional approach is mainly based on a 3-D spatial correlation, as shown in Eq. 3, to obtain the statistical peak, and, hence, to determine the mean particle displacement:

$$C(x,y,z) = \int \int_{Volume} \int f(\xi,\eta,\zeta) g(x-\xi, y-\eta, z-\zeta) \mathrm{d}\xi \mathrm{d}\eta \mathrm{d}\zeta \tag{3}$$

The process is usually complex while coping with more than two other dimensions, as expressed in the left term of Eq. 2. An alternative solution is the CCC algorithm, which correlates the two images one axis at a time, so that the process is simplified and saves a lot of time. A virtual intensity function that contributes to the particles in the first 3-D image is modeled as:

$$f(x,y,z) = \sum_{i=1}^{m} \mu_i(x,y,z) = \sum_{i=1}^{m} \exp\left[\frac{-\delta_i(x,y,z)^2}{2r^2}\right] \tag{4}$$

where $\delta_i(x,y,z)^2 = (x-x_i)^2 + (y-y_i)^2 + (z-z_i)^2$ and $r$ is defined as the radius of a particle. The same fashion



Fig. 5 Trend of diffraction efficiency of 12 recorded holograms with constant exposure energy 11.1 mJ/cm$^2$ and area of 1.13 mm$^2$
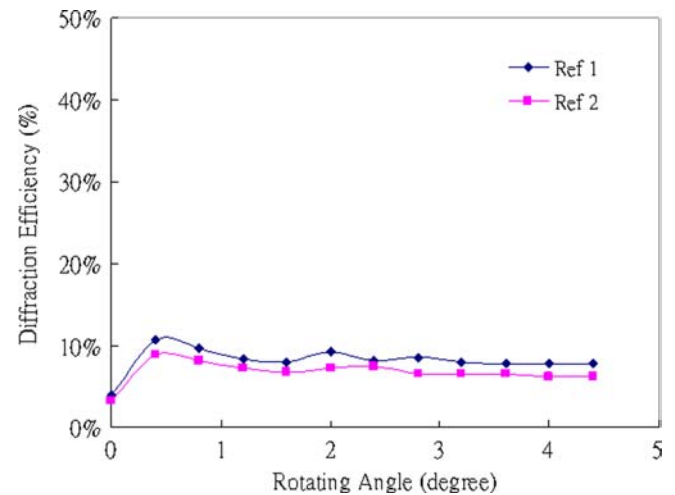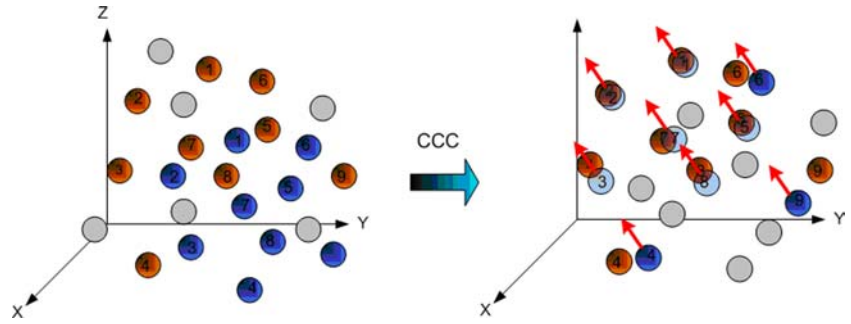


Fig. 6 A case of improved diffraction efficiency with properly adjusted exposure energy and exposure area. The image discriminability was maintained quite well for all holograms

can apply to the second image as well, obtaining $g(x,y,z) = \sum_{j=1}^{n} \mu_j(x,y,z)$. The function in Eq. 3 with such constructed models thus can reformulate as Eq. 5:

$$C(x,y,z) = \sum_{i=1}^{m} \sum_{j=1}^{n} \Gamma_{ij}(x,y,z;r) \tag{5}$$

where $m$, $n$ ($m = n$) are the number of particles in the first and second holograms, respectively. $\Gamma_{ij}$ is defined as a correlation kernel function for the discrimination of particles displacement relation:

$$\Gamma_{ij}(x,y,z;r) = \exp \left\{ - \frac{[x-(x_i-x_j)]^2 + [y-(y_i-y_j)]^2 + [z-(z_i-z_j)]^2}{2r^2} \right\} \tag{6}$$

To simplify the computation, the original 3-D model, Eqs. 5 and 6, can be decomposed into three 1-D correlation kernel functions, where each coordinate component is subject to the same particle, of which is expressed as:

$$C(x,y,z) = \sum_{i,j=1}^{m} \Gamma_{ij}(x)\Gamma_{ij}(y)\Gamma_{ij}(z) \tag{7}$$

where $\Gamma_{ij}(x) \equiv \Gamma_{ij}(x;r), \Gamma_{ij}(y) \equiv \Gamma_{ij}(y;r)$, and $\Gamma_{ij}(z) \equiv \Gamma_{ij}(z;r)$. If the statistical peak occurs when image 2 matches image 1, with a shift of $(x_0, y_0, z_0)$, the correlation along each axis can be assumed to obtain a peak at $x_0$, $y_0$, and $z_0$, respectively. For instance, a concise correlation for the $x$ axis can be expressed as:

$$C(x, y_0, z_0) = \chi \sum_{i,j=1}^{m} \Gamma_{ij}(x) \tag{8}$$

where $\chi = \Gamma_{ij}(y_0)\Gamma_{ij}(z_0)$ is a constant. A similar expression holds true for $C(x_0, y, z_0)$ and $C(x_0, y_0, z)$ as well, so that the remaining correlations corresponding to the same particle can be derived completely. Note that, although the CCC algorithm simplifies the complexity of a 3-D correlation, it could also decrease the ratio of successful particle pairings because of unsatisfied discriminability and confined interrogation cells.

## 2.5 Straight channel and backward facing step chamber

Two different flow patterns were investigated. The inner free flow in a straight microchannel was measured as a feasibility test. As shown in Fig. 8, the flow with suspended microspheres between two glass slices formed a space for preliminary investigation. The cross section was of dimensions 500 μm×30 μm.

The BFS chamber employed was developed by Chiu et al. (1998), as shown in Fig. 9, which has been used to simulate blood flow near arterial branches and bends. The chamber was composed of a base plate (dimensions 50×36×10 mm), an inlet valve, an outlet valve, a vacuum valve, two silicon rubber gaskets, and a coverslip that was 210-μm thick, as shown in Fig. 9a. The base was drilled with two holes with slits in both sides for the flow entrance and exit. The vacuum valve connected to a rectangular groove was fabricated for suction. A chamber with two different heights was formed by inserting two 250-μm gaskets with clear apertures of size 15×10 mm and 45×10 mm between the coverslip and the base. Afterwards, the coverslip and the gaskets were then sealed to the base plate by using a vacuum suction that formed a chamber, which is 10-mm wide (W), 250-μm high at the entrance section (h), and 500-μm high at the main section (H). The entrance length and the total length are 15 mm and 45 mm, respectively. The sketched flow pattern and computational fluid dynamics (CFD) simulated result is shown in Fig. 9b, c.

Fluid that flowed through the chamber was seeded with marker particles (diameter 1 μm, D-0100, Duke
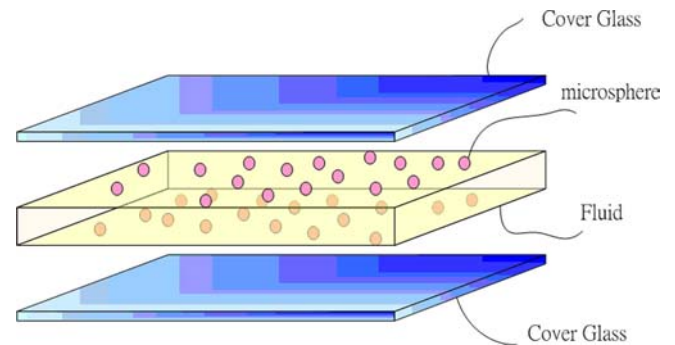


**Fig. 8** Structure of straight channel for preliminary investigation
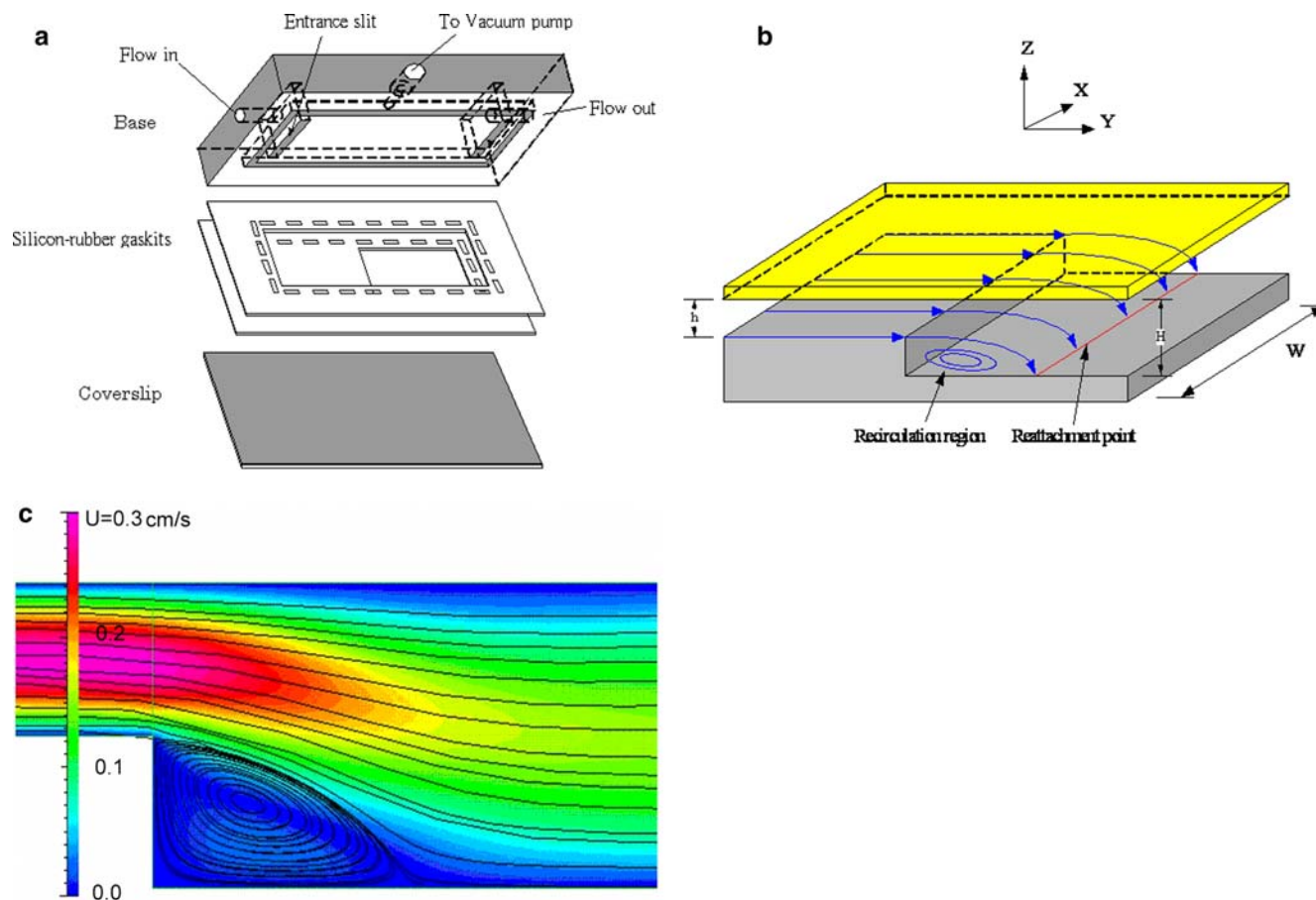
**Fig. 9a–c** Perspective diagram of the flow chamber. **a** Detailed decomposition of the vertical backward facing step (BFS) chamber. **b** A sketch of the flow pattern. **c** Computational fluid dynamics (CFD) simulation result (Yang et al. 2002)

Scientific, CA, USA), and the flow rates were 0.1 mL/min and 0.3 mL/min ($Re = 0.3$ and 0.9), respectively. The particle solution was diluted and stirred in advance to avoid serious particle overlaps, which could have hindered efficient discrimination. Typically, the chamber was categorized into four regions based on flow patterns: stagnation, recirculation, reattachment, and the fully development area. Flow in the reattachment region and the fully developed area was measured and is demonstrated in the discussion later.

### 2.6 MicroPIV measurement

A microPIV technique (Santiago et al. 1998; Chuang and Yang 2001) was also used to measure the same flow field for evaluating the performance of the new method. A steady 3-D flow field can be measured by using a microPIV with a plane-by-plane scanning scheme, so as to serve as a comparison reference. The flow field at 8 mm downstream of the step was selected for this reason.

First, the field of view was focused on the bottom of the chamber and was then stepped upward with an increment of 10 μm. To eliminate the uncertainty due to Brownian motion and other spurious errors, five image pairs were ensemble averaged over the same area for each measurement. The time interval between two instantaneous images was 10 ms, while the microflow images were acquired with 15-fold magnification. In addition, the seeding density was very low in the measurements to keep good particle discriminability for the purpose of demonstrating the feasibility of the proposed holographic setup at the present phase. Therefore, the interrogation window in calculating microPIV measurement results was selected as large as 128×256 pixels, with an overlap ratio of 50%.

## 3 Results and discussions

To verify the performance of the present setup, the measurements of flow in a straight microchannel were conducted beforehand. The vertical BFS chamber was measured for its flow field near the reattachment region. Also, the measurement results using a calibrated microPIV were utilized to evaluate the new method for further improvement. Plus, we adopted a chromatic approach based on a diffraction operation to facilitate the flow visualization.

## 3.1 Preliminary study

Fluid dropped into the channel, as shown in Fig. 8, formed a free flow. The flow was measured with the following parameter settings: $\Delta t = 100$ ms, $T = 1$ s, light intensity of each beam $\approx 25$ mW, and the exposure time for each hologram $\approx 3$ ms. In the image-retrieving process, the total scanning depth was about 19.5 μm, with an increment of 0.65 μm, and the field of view was $232 \times 186$ μm. Raw image pairs scanned at the middle plane of the channel are shown in Fig. 10a. The extracted particle distribution in a local region of image pair 1:1 and 1:2 is shown in Fig. 10b. To enhance discriminability, the particle concentration was controlled to avoid apparently reciprocated interference. The current probability of successful pairing was estimated at <60%.

The PTV and CCC algorithms were both applied in calculating the 3-D velocity field. The result analyzed by using PTV approach is shown in Fig. 11, and the calculated mean velocity was 9.18 μm/s. This result served as a reference. For the CCC algorithm, an ensemble average was required, and spurious vector removal,

interpolation, and smoothing were implemented in the post processing. The ensemble average result of the same region by using the CCC algorithm is shown in Fig. 12, in which streamwise velocities coincided with simulated laminar flow profiles in rectangular channels. The streamwise velocity distribution in about 1/4 of the cross section is shown in Fig. 13. The streamwise velocity around the central region of the channel is 12.2 μm/s, and the estimated average velocity matched the PTV result.

## 3.2 Flows in the microBFS chamber

To further verify the advantage of the new holographic method in getting transient, full-field 3-D velocity field, a vertical BSF chamber was employed. The test flow rate was 0.3 mL/min, and the reattachment occurred at some 100 μm downstream of the step. Because of its low aspect ratio (depth/width) of 0.05, the flow could be treated as 2-D, and we just performed the measurement along the central axis to characterize its flow pattern.

Because the travel distance of the linear stage was limited and the diffraction intensity was decayed along the optical axis, we focused the measurement in a region $232.5 \times 186 \times 71.5$ μm near the chamber bottom. The final three-dimensional, three-component (3D–3C) velocity

**Fig. 10 a** Raw image pairs scanned at middle plane of the channel. **b** Spatial distribution of discriminated particles. *Red dots* and *yellow dots* denote particles in images 1.1 and 1.2, respectively
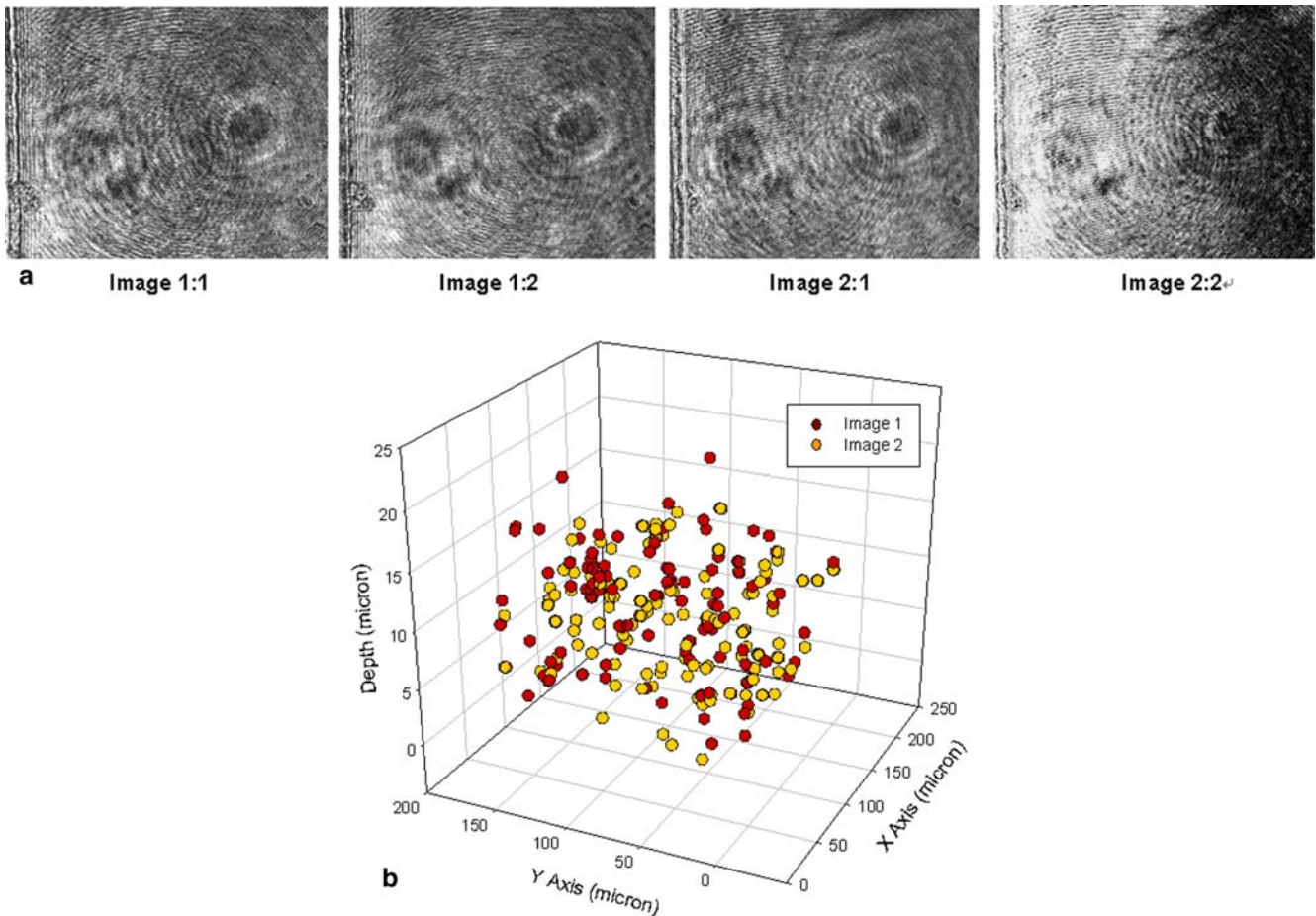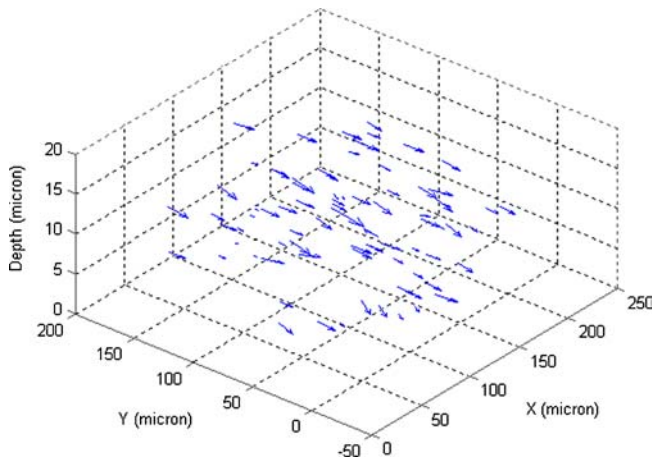
**Fig. 11** Velocity vector distributions using PTV method

vector map is shown in Fig. 14, in which the depth information of the velocity vectors were encoded by using colors. For instance, the velocity vectors near the observer were painted with colors of long wavelength; in contrast, vectors distant from the observer were painted with colors of short wavelength. Based on the diffraction theorem (Steenblik 1991), the locations of the vectors can be distinguished when wearing chroma 3-D glasses, i.e., red vectors appear close to the observer while blue vectors appear farther away. The chromatic technique, therefore, innovated an easy way to visualize a 3-D fluid flow from a velocity vector image like Fig. 14. If the velocity vector plots could be rotated and zoomed in and out arbitrarily, with vector colors changing according to their new coordinates, it would be helpful in understanding the flow field structure when designing microfluidics.

Different perspective views of the characteristic flow are exhibited in Fig. 15 for in-depth analysis. From the top view, the flow reattachment is estimated to be 614.4 μm downstream of the step at a flow rate of 0.3 mL/min. Side views and rear views illustrate a strong downward flow, which rapidly flows to the recirculation region and downstream, respectively, before touching the bottom.

### 3.3 System evaluation

The holographic velocimetry was evaluated for its accuracy and uncertainty by comparing it with micro-PIV results. The microPIV method was calibrated by using an interferometry and a high-precision linear stage in advance. The calibrated velocities ranged from 1 μm/s to 200 μm/s, while two 10× and 40× objectives were applied, respectively. According to the ISO GUM, the analysis indicated that the deviation between the measured results by using interferometry and microPIV was 0.4%, and that the relative expanded uncertainty was 1% at a 95% confidence level (Chuang and Yang 2003).
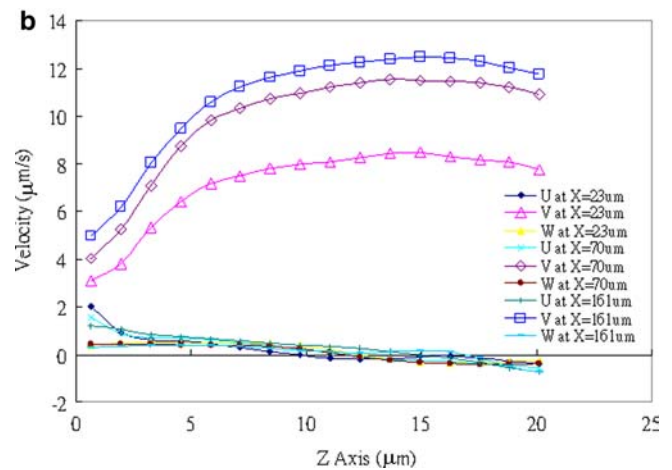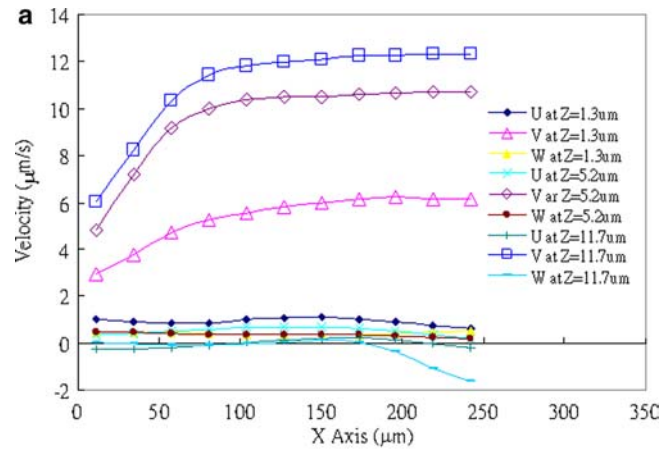


**Fig. 12a, b** Velocity profiles with respect to the $x$ and $z$ axes. The *squares*, *diamonds*, and *triangles* in both figures denote streamwise velocities ($V$) at three distances from the wall. The other symbols for lateral $U$ and $W$ velocities approach zero except near the walls. **a** Velocity profiles in the perspective of the $z$ direction. **b** Velocity profiles in the perspective of the $x$ direction
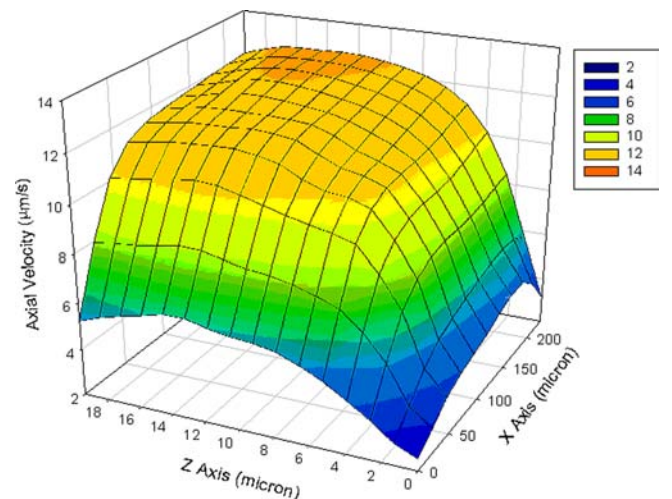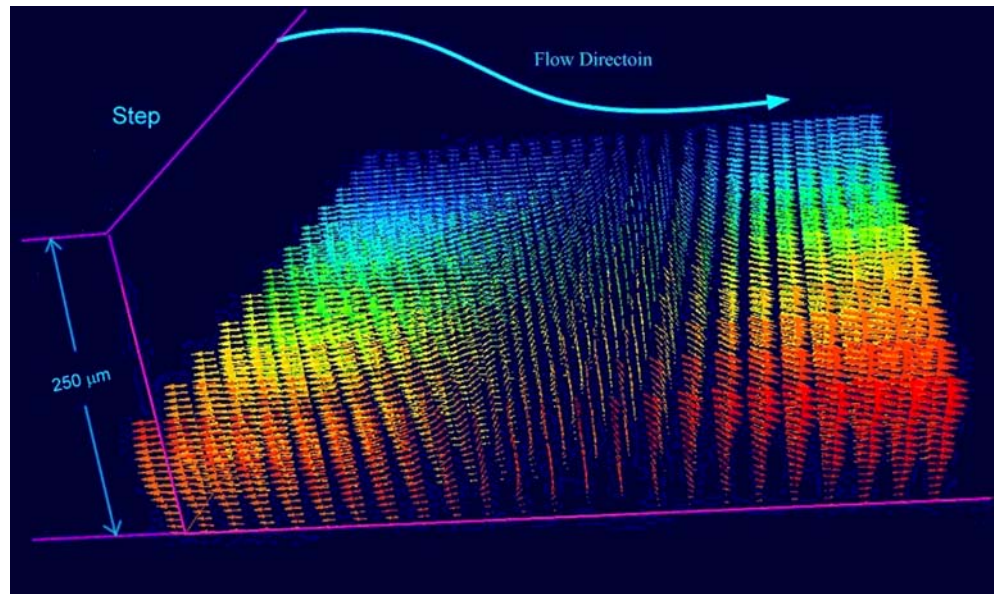


**Fig. 13** 2-D velocity map of 1/4 cross-section of the straight microchannel

**Fig. 14** A three-dimensional, three-component (3D–3C) velocity vector map of the flow in the region of reattachment at the flow rate of 0.3 mL/min (see Fig. 2)



Flow field at 8 mm downstream of the step, which was assumed to be fully developed and laminar, was measured by using the two velocimetries at a flow rate of 0.1 ml/min. The measurement results are shown in Fig. 16, in which the scanned depths showed a little difference. Extracted velocity profiles from Fig. 16 are shown in Fig. 17, in which the absolute deviation increases with the distance from the bottom. For instance, the holographic velocimetry obtained an average velocity of 370.4 μm/s at $z = 75$ μm; while a mean reference velocity by using microPIV was 333.4 μm/s. The average deviation was estimated to be 9% from the reference, implying that some uncertainties occurred in recording or reconstructing the spatial distribution of particles. The possible sources that influence the measurement accuracy and uncertainty include:
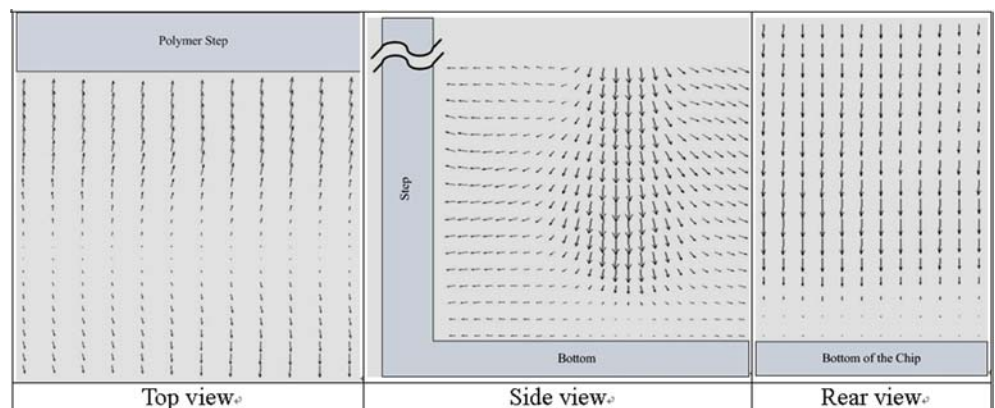
(1) The focal elongation induced from the magnification of the macro lens set obscured the exact discrimination of particle location along the $z$ axis. According to the past estimation, the uncertainty could be as large as 10%.

(2) Slight deviations existed between the reconstructed images when being diffracted by Ref 1 and Ref 2. Therefore, the distance mismatch should be removed before the calculations.

(3) The holograms were very sensitive to environment so that slight fluctuations of the rotation stage had contributed to a deviation in reconstructed images. It is concluded that strict control of the measurement environment should be enforced.

(4) The discrimination of the particles decreased when the forward scattering light resulted in strong background noise. Contrast improvement was, thus, essential. Eliminating the background noise by using a high-pass filter is under study to optimize the contrast.

## 4 Conclusions

In this paper, a state-of-the-art experimental method based on a hybrid multiplexing holography technique

**Fig. 15** Three perspective views of the characteristic flow section. The locations of the planes are $z = 0$ μm, $x = 160$ μm, $y = 112$ μm with respect to the diagrams from *left* to *right*
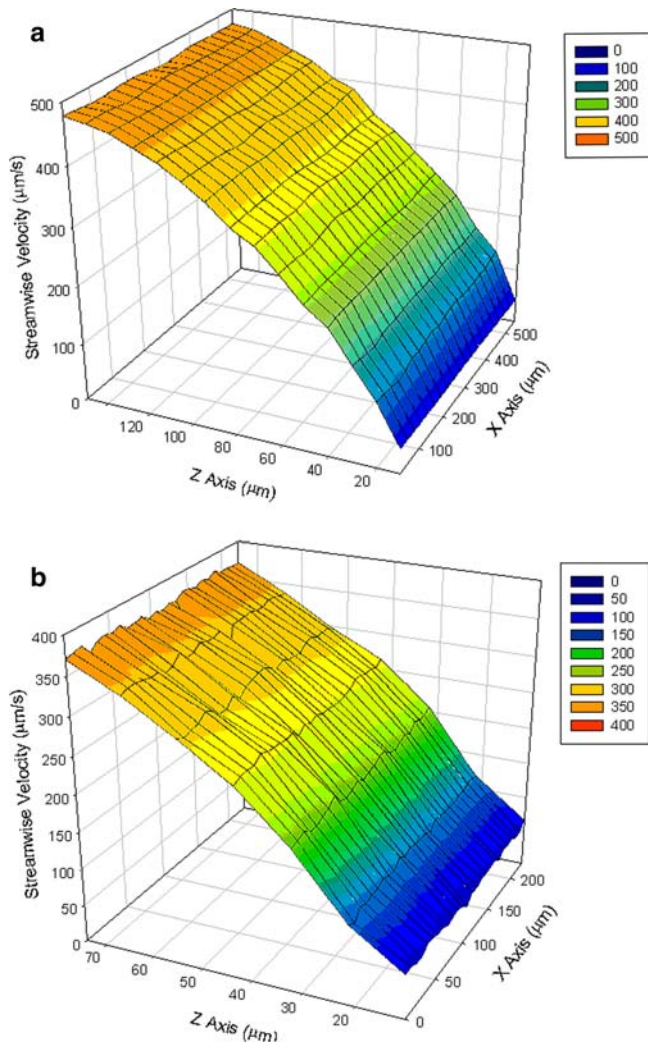
Fig. 16a, b Flow profiles at 8 mm downstream of the step by using **a** microPIV and **b** multiplexing holographic velocimetry, respectively



Fig. 17 Comparison of velocity measured by microPIV ($U\_PIV$) and holographic velocimetry ($U\_HV$) for accuracy evaluation

particle tracking velocimetry (PTV) and the CCC algorithm, respectively. The identical result proved the validity of the CCC algorithm. Afterwards, a backward facing step (BFS) chamber was investigated for its characteristic flow near the reattachment region. The results indicated that the present holographic velocimetry can effectively obtain 3D–3C flow characteristics in a microscopic space. We also presented a simple and easy approach to visualizing the stereo full-field flow by coloring the flow vectors according to a chromatic technique. Finally, measurements were made in a steady flow region at low $Re$ by using a holographic setup and a calibrated microPIV. The deviation implies that uncertainty sources occurred in the acquisition of the spatial distribution of the particles.

As a whole, the system was approved of its practicability by means of serial measurements and comparisons. However, improvements for increasing the discriminability of particles, reducing the background noise, ascertaining the repeatability of multiplexing operation, etc. are required to further enhance the measurement performance

## References

Arroyo PM, Andres N, Quintanilla M (2000) The development of full field interferometric methods for fluid velocimetry. Opt Laser Technol 32:535–542

Barnhart DH, Adrian RJ, Papen GC (1994) Phase conjugate holographic system for high resolution particle image velocimetry. Appl Opt 33:7159–7170

Chiu JJ, Wang DL, Chien S, Skalak R, Usami S (1998) Effects of disturbed flow on endothelial cells. J Biomech Eng 120:2–8

Chiu JJ, Chen CN, Lee PL, Yang CT, Chuang HS, Chien S, Usami S (2003) Analysis of the effect of disturbed flow on monocytic adhesion to endothelial cells. J Biomech 36:1883–1895

was proposed for three-dimensional, three-component (3D–3C) micro-fluidic measurement. Derived from the holographic particle image velocimetry (HPIV) concept, the system consisted of holographic multiplexing, a new recording medium, a microscopy, and a concise cross-correlation (CCC) algorithm. In the hologram-recording process, the required extra-short time interval between two successive images was determined by using a non-mechanical optical modulator; while the time interval between two image pairs was determined by mechanically rotating the recording medium. By adopting the CROP photopolymer, the system captured and stored several tens of image pairs simultaneously with the exposure time down to 3 ms for each recording. Aside from this, the criteria for obtaining distinguishable holograms from successive recordings were also investigated.

First, the flow in a straight microchannel was investigated. The reconstructed images were analyzed by both
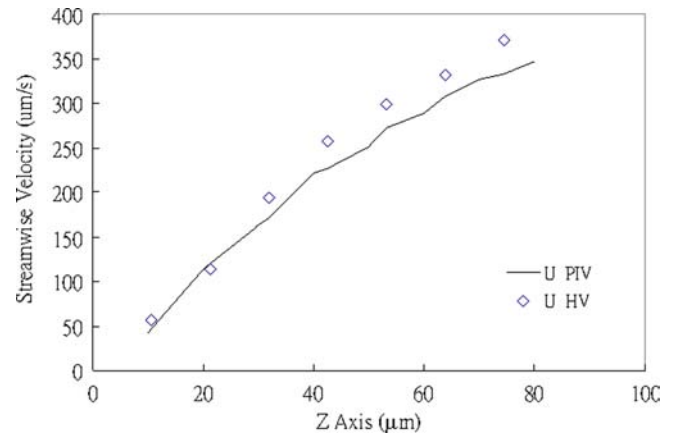
Chuang HS, Yang CT (2001) Micro flow measurement in a capillary with a diode laser micro-PIV. In: Proceedings of the 5th nano engineering and micro system technology workshop, Hsinchu, Taiwan, November 2001, pp 4-95–4-101

Chuang HS, Yang CT (2003) Evaluation of a micro-PIV based on a special calibration design. Technical report no. 073920029, Center for Measurement Standards, Industrial Technology Research Institute (CMS/ITRI), Taiwan

Clark KL (1973) Negations as failure, in logic and data bases. In: Gallaire H, Winker J (eds) Plenum Press, New York, pp 293–306

Coupland JM, Halliwell NA (1992) Particle image velocimetry: three-dimensional fluid velocity measurements using holographic recording and optical correlation. Appl Opt 31:1004–1008

Cuche E, Parquet P, Depeursinge C (1999) Simultaneous amplitude–contrast and quantitative phase–contrast microscopy by numerical reconstruction of Fresnel off-axis holograms. Appl Opt 38:6994–7001

Dubois F, Joannes L, Legros JC (1999) Improved three-dimensional imaging with a digital holography microscope with a source of partial spatial coherence. Appl Opt 38:7085–7094

Hinsch KD (2002) Holographic particle image velocimetry. Meas Sci Technol 13:R61–R72

Inoué S, Spring K (1997) Video microscopy: the fundamentals. Plenum Press, New York

Kawahashi M, Hirahara H (2001) A new technique of three-dimensional particle image detection by using color encoded illumination system. In: Proceedings of the 4th international symposium on particle image velocimetry (PIVOT), Göttingen, Germany, September 2001, pp 1061-1–1061-7

Ken YH, Lin SH, Hsiao YN (2003) Experimental characterization of phenanthrenequinone-doped poly(methylmethacrylate) photopolymer for volume holographic storage. Opt Eng 42(5):1390–1396

Lozano A, Kostas J, Soria J (1999) Use of holography in particle image velocimetry measurements of a swirling flow. Exp Fluids 27:251–261

Ovryn B (2000) Three-dimensional forward scattering particle image velocimetry applied to a microscopic field-of-view. Exp Fluids 29:S175–S184

Pan M, Meng H (2001) Digital in-line holographic PIV for 3D particulate flow diagnostics. In: Proceedings of the 4th international symposium on particle image velocimetry (PIVOT), Göttingen, Germany, September 2001, pp 1008-1–1008-7

Paraschis L, Sugiyama Y, Hesselink L (1999) Physical properties of volume holographic recording utilizing photo-initiated polymerization for nonvolatile digital data storage. SPIE 3802:72–83

Pu Y (2002) Holographic particle image velocimetry: from theory to practice. PhD thesis, pp 63–88

Pu Y, Meng H (2000) An advanced off-axis holographic particle image velocimetry (HPIV) system. Exp Fluids 29:184–197

Royer H (1997) Holographic and particle image velocimetry. Meas Sci Technol 8:1562–1572

Santiago JG, Wereley ST, Meinhart CD, Adrian RJ (1998) A micro particle image velocimetry system. Exp Fluids 25:316–319

Schnars U, Jüptner W (1994) Direct recording of holograms by a CCD target and numeral reconstruction. Appl Opt 33:179–181

Steenblik RA (1991) Stereoscopic process and apparatus using different deviation of different colors. US Patent no. 5002364

Waldman DA, Li H-YS, Cetin EA (1998) Holographic recording properties in thick films of ULSH-500 photopolymer. SPIE 3291:89–103

Xu W, Jericho MH, Meinertzhagen IA, Kreuzer HJ (2001) Digital in-line holography for biological applications. Proc Natl Acad Sci USA 98:11301–11305

Yang CT, Chuang HS, Chen, JY, Chiu JJ (2002) Microscopic flow behind a backward facing step—a model analysis for cell adhesion study. In: Proceedings of the 10th international symposium on flow visualization, Kyoto, Japan, August 2002, p 23

Zhang J, Tao B, Katz J (1997) Turbulent flow measurement in a square duct with hybrid holographic PIV. Exp Fluids 23:373–381